


Enhanced Electrical Properties of $\text{Bi}_{2-x}\text{Sb}_x\text{Te}_3$ Nanoflake Thin Films Through Interface Engineering

Xudong Wu, Junjie Ding, Wenjun Cui, Weixiao Lin, Zefan Xue, Zhi Yang, Jiahui Liu, Xiaolei Nie, Wanting Zhu, Gustaaf Van Tendeloo, and Xiaohan Sang* 


The structure–property relationship at interfaces is difficult to probe for thermoelectric materials with a complex interfacial microstructure. Designing thermoelectric materials with a simple, structurally-uniform interface provides a facile way to understand how these interfaces influence the transport properties. Here, we synthesized $\text{Bi}_{2-x}\text{Sb}_x\text{Te}_3$ ($x = 0, 0.1, 0.2, 0.4$) nanoflakes using a hydrothermal method, and prepared $\text{Bi}_{2-x}\text{Sb}_x\text{Te}_3$ thin films with predominantly (0001) interfaces by stacking the nanoflakes through spin coating. The influence of the annealing temperature and Sb content on the (0001) interface structure was systematically investigated at atomic scale using aberration-corrected scanning transmission electron microscopy. Annealing and Sb doping facilitate atom diffusion and migration between adjacent nanoflakes along the (0001) interface. As such it enhances interfacial connectivity and improves the electrical transport properties. Interfacial reactions create new interfaces that increase the scattering and the Seebeck coefficient. Due to the simultaneous optimization of electrical conductivity and Seebeck coefficient, the maximum power factor of the $\text{Bi}_{1.8}\text{Sb}_{0.2}\text{Te}_3$ nanoflake films reaches $1.72 \text{ mW m}^{-1} \text{ K}^{-2}$, which is 43% higher than that of a pure Bi_2Te_3 thin film.

1. Introduction

Physical and mechanical properties of materials often critically depend on the microstructure and properties of the interfaces. Researchers now have the ability to design and construct an individual interface using epitaxial growth techniques or layer-by-layer stacking for 2D materials,^[1–4] and then correlate the emergent magnetic,^[5–7] electronic,^[8,9] ferroelectric,^[1,10] superconducting,^[11] and other quantum properties, with the interfacial structure at the atomic and electronic level. However, clear interfacial structure–property relationships

X. Wu, J. Ding, W. Cui, W. Lin, Z. Xue, Z. Yang, J. Liu, Prof. X. Sang
State Key Laboratory of Advanced Technology for Materials Synthesis and Processing, Wuhan University of Technology, Wuhan 430070, China
E-mail: xhsang@whut.edu.cn

X. Wu, J. Ding, W. Cui, W. Lin, Z. Xue, Z. Yang, X. Nie, W. Zhu, Prof. G. Van Tendeloo, Prof. X. Sang
NRC (Nanostructure Research Centre), Wuhan University of Technology, Wuhan 430070, China
Prof. G. Van Tendeloo
EMAT (Electron Microscopy for Materials Science), University of Antwerp, Groenenborgerlaan 171, Antwerp 2023, Belgium

 The ORCID identification number(s) for the author(s) of this article can be found under <https://doi.org/10.1002/eem2.12755>.

DOI: 10.1002/eem2.12755

are extremely difficult to achieve as most bulk materials and films contain various types of interfaces with different orientation, chemical composition or defect structure. Synthesizing materials with more structurally-uniform interfaces can therefore help to increase the impact of a particular interface on the overall properties, and realize the potential of interface engineering in material science.^[12–14]

Thermoelectric (TE) materials enable direct conversion between thermal and electrical energy, providing a straight-forward solution to recycle waste heat in industry. TE energy conversion efficiency can be described using the dimensionless factor $ZT = (\alpha^2 \sigma / \kappa) T$, where α is the Seebeck coefficient, σ the electrical conductivity, κ the thermal conductivity and T the absolute temperature.^[15,16] High TE efficiency requires the combination of transport properties such as low κ , high α and σ . However, these parameters are intrinsically correlated, and so far, it has been extremely difficult to further increase ZT values through conventional approaches such as defect engineering^[17] and

band engineering.^[18–20] As the interfaces within bulk or thin film TE materials provide additional scattering mechanisms for electron and phonon transport,^[21–23] it is expected that building TE materials with specific interfaces can enhance the TE properties,^[24–27] and is also beneficial for TE devices.^[28,29]

Bi_2Te_3 -based alloys are the most widely investigated TE materials due to a high power factor and low thermal conductivity.^[7,13,30,31] Bi_2Te_3 (BT) has a strongly anisotropic layered structure with better transport properties along the in-plane than the out-of-plane direction, providing an ideal example to study the influence of interface engineering on the overall TE properties. It has been reported that enhanced electrical properties of BT-based thin films can be achieved by Sb-doping or improving the growth method.^[32–37] Here, a series of Sb-doped $\text{Bi}_{2-x}\text{Sb}_x\text{Te}_3$ (BST) ($x = 0, 0.1, 0.2, 0.4$) nanoflakes were synthesized and spin-coated to form BST thin films with predominantly (0001)-terminated interfaces. Using scanning transmission electron microscopy (STEM), the atomic structure of the (0001) interfaces in BST thin films with different composition and annealed at different temperatures have been investigated. Annealing and Sb-doping noticeably increases the connection between the nanoflakes, which simultaneously enhances α and σ . The maximum power factor reaches $1.7 \text{ mW m}^{-1} \text{ K}^{-2}$ at 350 K, which is the highest among n-type TE thin films prepared from BT nanoflakes.^[31]

2. Results and Discussion

BST has a rhombohedral layered crystal structure (space group $R\bar{3}m$) consisting of $\text{Te}^{(1)}\text{-Bi-Te}^{(2)}\text{-Bi-Te}^{(1)}$ quintuple layers that are separated by weak van der Waals (vdW) forces between the terminating Te sublayers. Within the quintuple layer, the Bi and Te atoms are covalently bonded. Electron transport along the vdW gap is much easier than perpendicular to the vdW gap. The in-plane σ to out-of-plane σ ratio ranges from 4 to 7 for n-type BST single crystals.^[38] Therefore, to optimize the in-plane electron transport properties of BST thin films, it is desirable to have the c axes of the BST grains perpendicular to the film surface, forming a (0001)-textured microstructure. We synthesized BST hexagonal nanoflakes with large width/height ratio using a hydrothermal method, and then stacked them using spin coating to form thin films with nanoflakes that are preferentially

parallel to the thin film surface (Figure 1a, see Section 4 for more details).

The as-synthesized BST nanoflakes have a hexagonal shape as characterized using field emission scanning electron microscopy (FESEM) (Figure 1b). The BST nanoflake diameter ranges roughly from 400 to 800 nm (Figure S1, Supporting Information). Sb doping does not noticeably influence the morphology or size of the nanoflakes (Figure S1, Supporting Information). The X-ray diffraction (XRD) peaks match well with the BT rhombohedral crystal structure (JCPDS 01-083-5986) (Figure S2, Supporting Information). With increasing Sb content, the (01 $\bar{1}$ 5) diffraction peak shifts from 27.4° to 27.9°, indicating that the substitution of the smaller Sb cations on the Bi sites causes the lattice constants to decrease. Sb substitution on the Bi sites was also verified by X-ray photoelectron spectroscopy (XPS) (Figure S3, Supporting Information) where the Sb 3d peak can be

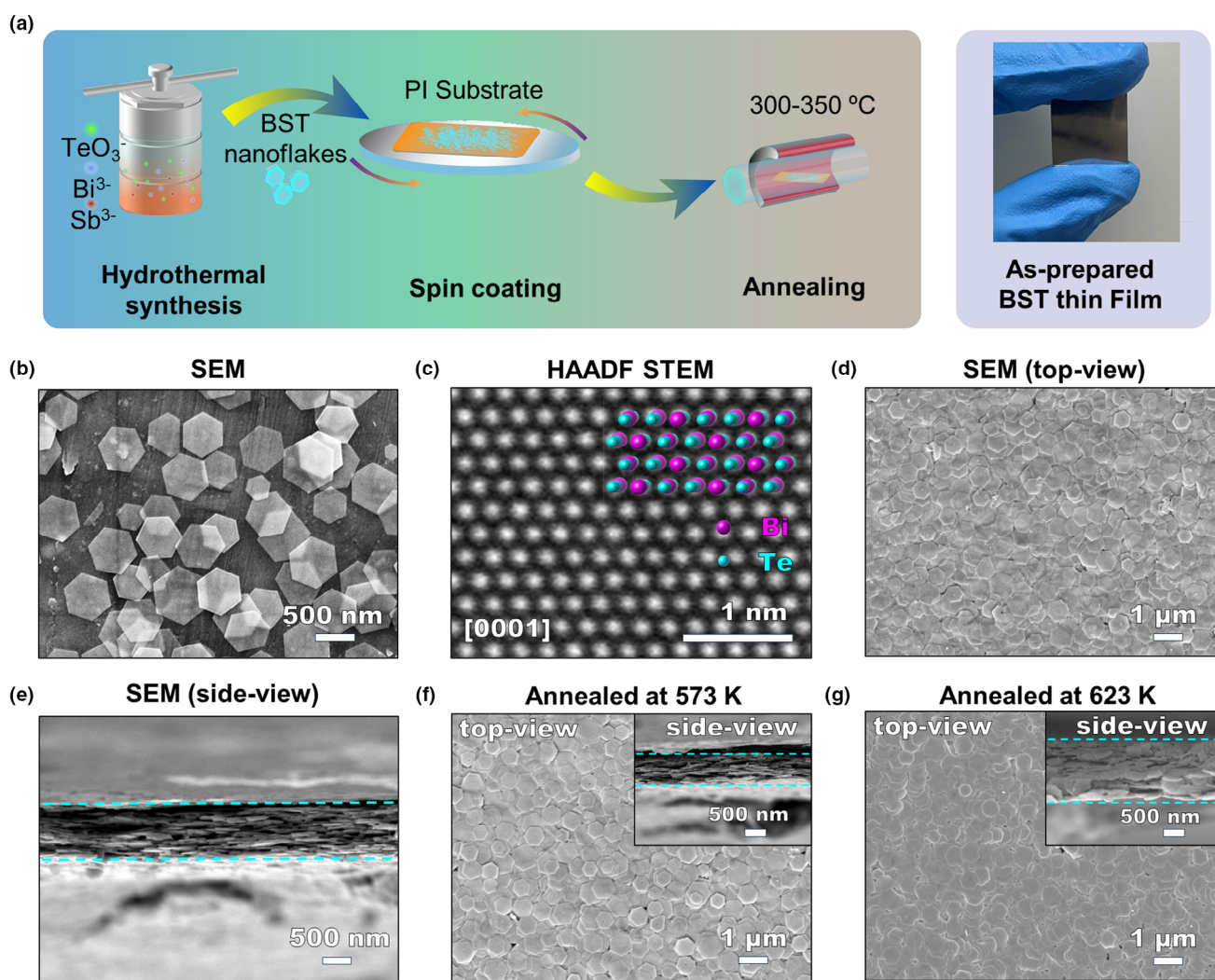


Figure 1. a) The schematic of the BST thin film preparation process. b) Typical SEM image of dispersed $\text{Bi}_{2-x}\text{Sb}_x\text{Te}_3$ nanoflakes with $x=0.2$. c) Atomic-resolution HAADF STEM image acquired along the c axis of BST. The projected crystal structure is slightly tilted to show that the atomic columns have mixed Bi (purple) and Te (cyan) atoms. Top-view d) and side-view e) SEM image of a BST thin film with $x=0.2$. Top-view and side-view (insets) SEM images of Bi_2Te_3 (BT) thin film annealed at f) 573 K and g) 623 K.

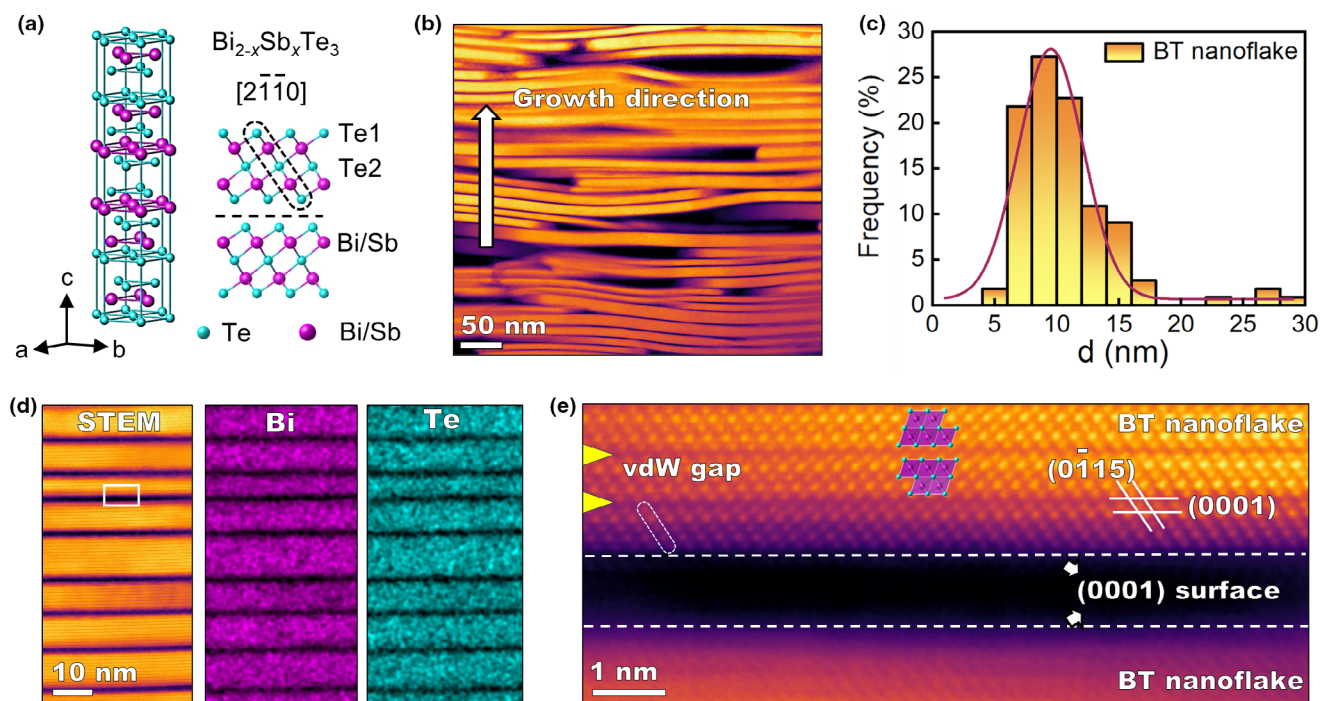


Figure 2. a) Atomic model of the $\text{Bi}_{2-x}\text{Sb}_x\text{Te}_3$ (BST) crystal structure. b) HAADF STEM image of a cross-section BT thin film, where the white arrow indicates the deposition direction. c) Distribution of the (as-prepared) BT nanoflake thickness d . d) Electron dispersive spectroscopy (EDS) mapping acquired from the BT thin film. e) Atomic-resolution HAADF STEM image acquired from the rectangle framed in d), imaged along the $[2\bar{1}\bar{1}0]$ zone axis. The two (0001) surfaces are indicated by white arrows. Crystallographic planes are indicated by white lines. Two vdW gaps are denoted by yellow arrows. A quintuple-layer structure is encircled by a white dashed rod.

observed. An atomic-resolution high angle annular dark field (HAADF) STEM image, acquired along the c axis of the nanoplate, shows the hexagonal pattern of the Bi/Te mixed atomic columns, consistent with the projected crystal structure (Figure 1c). HAADF STEM intensities are proportional to the average projected atomic number,^[39] and are extensively used in this work to probe the atomic structure at the interfaces.

The BST nanoflakes were dispersed in anhydrous ethanol and then spin-coated onto the polyimide substrate to form a continuous and flexible BST thin film. The top-view SEM image of a BST thin film with $x = 0.2$ (Figure 1d) reveals that all the hexagonal nanoflakes are lying flat on the surface. The BST film thickness is roughly 900 nm as confirmed by cross-sectional SEM (Figure 1e). Across the thickness, all nanoflakes are parallel to the surface, such that two stacked nanoflakes always connect through their (0001) surfaces. Therefore, the key to understand the transport properties of the BST thin film is to understand the structure and properties of the interconnecting flakes and particularly the interconnecting (0001) surfaces and interfaces. As-prepared BST thin films were then annealed at different temperatures (573–623 K) in order to modify the interfacial structure. Annealing at 573 K does not noticeably change the morphology of the BT thin film (see the low-magnification SEM image in Figure 1f). However, when annealing at 623 K we observed a significant intergranular diffusion and coarsening (Figure 1g). Annealing at even higher temperature (673 K) can significantly alter the shape of nanoflakes, which complicates interface structure and thus structure–property relationship. Therefore, the highest annealing temperature was set to 623 K.

We first investigated the (0001) interfacial structure in an as-prepared BT thin film at atomic resolution using STEM. Cross-sectional samples were fabricated using focused ion beam (FIB). The stacking of the nanoflakes is clearly visible in the low-magnification HAADF STEM image (Figure 2b), where each rod-shaped region represents the cross-section of a BT nanoflake. Direct measurement from STEM images (Figure S4a, Supporting Information) suggests that the BT nanoflake thickness is about 11 ± 4 nm (Figure 2c). Electron dispersive spectroscopy (EDS) elemental mapping shows that Bi and Te elements are evenly distributed in the nanoflakes, but are absent in the dark regions between the flakes (Figure 2d). The space between adjacent nanoflakes is due to surface steps resulting from the nanoflake growth around a Te nanorod or a screw dislocation in the center.^[40] The pressure from spin coating is insufficient to deform surface steps. Atomic-resolution HAADF STEM images acquired along the BT $[2\bar{1}\bar{1}0]$ zone axis of one nanoplate clearly show the quintuple-layered structure (Figure 2e). The brighter dots are Bi atomic columns and the weaker dots are Te atomic columns, as Bi atom is heavier than Te.^[41–45] Note that the adjacent nanoflake is also oriented close to the $[2\bar{1}\bar{1}0]$ zone axis, hinting that adjacent nanoflakes tend to have a small twist angle, which could be arising from electrostatic forces. This small twist angle is occasionally observed on top-view SEM images (Figure S5, Supporting Information). The terminating quintuple layers of both plates, show no trace of interfacial reaction or surface reconstruction, which however has been commonly observed in BT surfaces exposed to air^[46,47] or at the interfaces between BT and transition metal elements such as Ni.^[48,49] We can conclude that in an unannealed BT thin film the

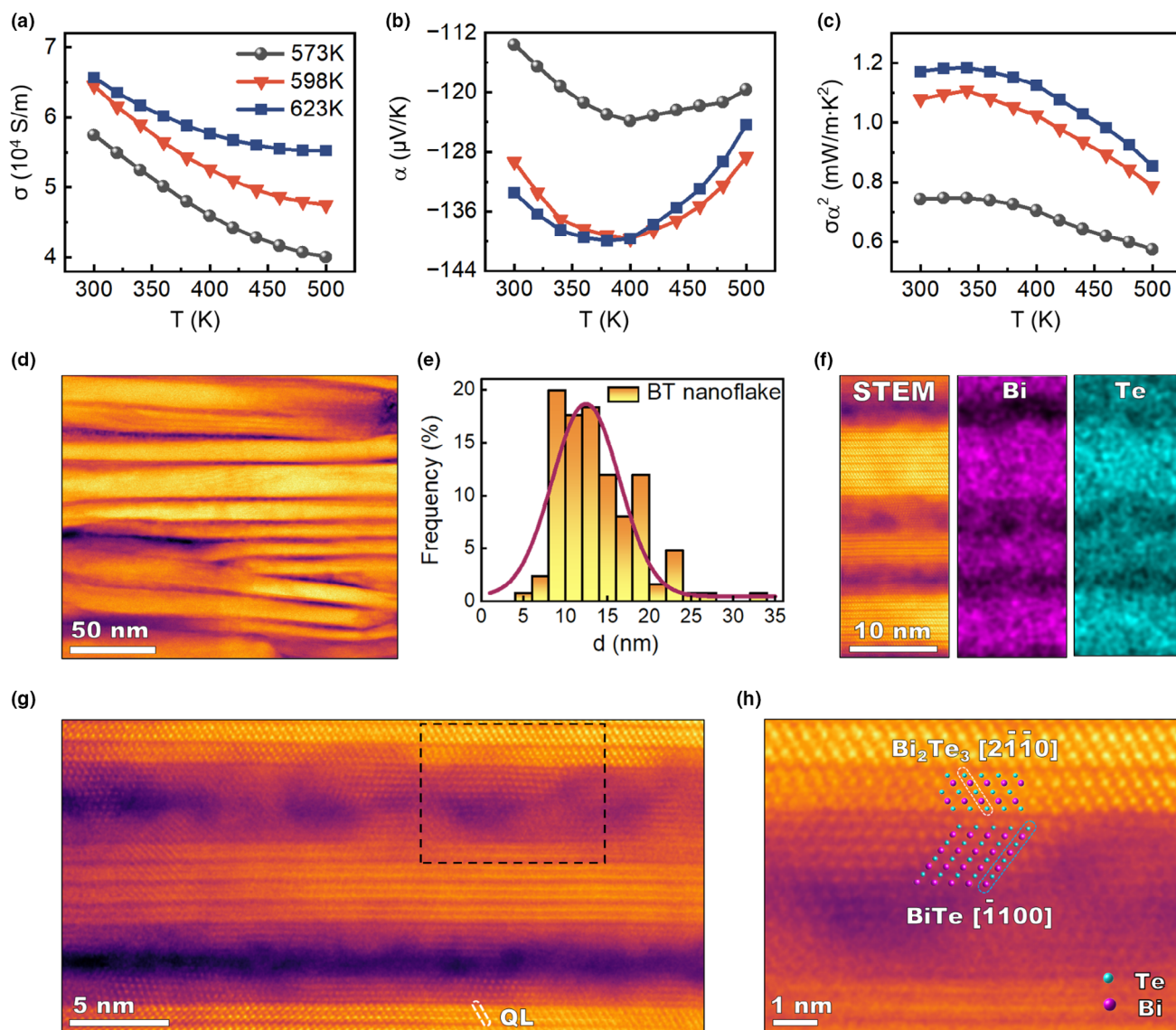


Figure 3. Experimental electrical transport properties of BT thin films annealed at different temperatures. a) Conductivity. b) Seebeck coefficient. c) Power factor. d) HAADF STEM image of a cross-sectional BT thin film annealed at 623 K. e) Thickness histogram of the nanoflakes in the BT film annealed at 623 K. f) EDS maps of the nanoflakes and the interfaces of the annealed BT thin film. g) Atomic-resolution HAADF STEM image acquired along the BT $[2\bar{1}\bar{1}0]$ zone axis. h) Enlarged HAADF STEM image from the black box in g).

flakes are terminated by stable (0001) surfaces separated by voids. Adjacent flakes do not react with each other.

The non-interacting nanoflakes in as-prepared BT thin films lead to a lower electrical conductivity σ ($0.36 \times 10^4 \text{ S m}^{-1}$) and Seebeck coefficient α ($100 \mu\text{V K}^{-1}$) (Figure S6, Supporting Information), compared with BT thin films annealed at 573–623 K (Figure 3a,b). As the annealing temperature increases, the room temperature σ of the BT thin film increases from 5.75×10^4 to $6.6 \times 10^4 \text{ S m}^{-1}$, and the maximum α increases from -124 to $-140 \mu\text{V K}^{-1}$, achieving a simultaneous improvement of α and σ . As a result, the maximum power factor reaches $1.2 \text{ mW m}^{-1} \text{ K}^{-2}$ at 343 K for a BT thin film annealed at 623 K. For all three samples, the negative-temperature dependence of the electrical conductivity and negative Seebeck coefficients indicate that BT films are n-type degenerate semiconductors. This could be explained

by donor-like effect caused by oxidation during sample preparation.^[50] The large surface to volume ratio makes thin films more prone to be oxidized.

After annealing at 623 K, the nanoflake thickness becomes less homogeneous (Figure 3d). Statistical analysis suggests that the thickness histogram (Figure 3e) has shifted to the right with an average thickness of 14 nm compared with the 11 nm before annealing (Figure 2c). The (0001) interface shows a blurred contrast, which is very different from the as-prepared sample where the gap is clean. EDS mapping reveals a Bi and Te signal at the gap between the nanoflakes (Figure 3f), indicating that Bi and Te atoms migrate between the nanoflakes during annealing. The quintuple layer at the interface has evolved to a different crystal structure (Figure 3g,h), which matches well with the face centered cubic (fcc) BiTe crystal structure viewed along the

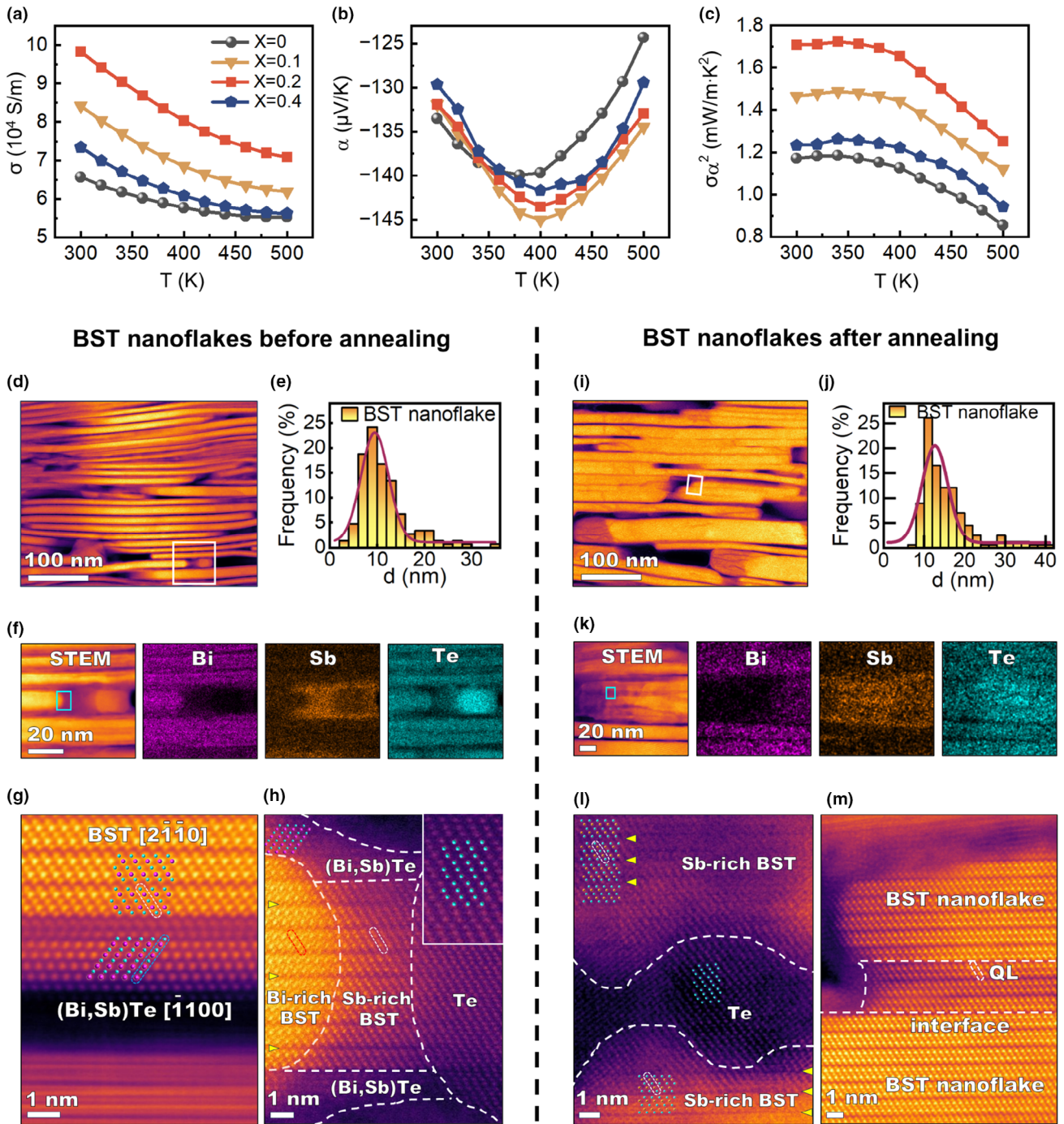


Figure 4. Electrical transport properties of the annealed BST thin films with different Sb content: a) Conductivity. b) Seebeck coefficient. c) Power factor. d) HAADF STEM image of the as-prepared BST thin film with $x=0.2$. e) The corresponding nanoflake thickness histogram of the as-prepared BST thin film. f) EDS mappings of as-prepared BST thin film. g) HAADF STEM image showing epitaxial BiTe at the (0001) interface in as-prepared BST. h) HAADF STEM showing the formation of pure Te at one end of a BST nanoplate. The inset compares the projected Te atomic columns and the crystal structure along the [2 $\bar{1}$ 10] zone axis. i) HAADF STEM image of the BST thin film annealed at 623 K. j) The corresponding nanoflake thickness histogram of the annealed BST thin film. k) EDS maps of the annealed BST thin film. l) HAADF STEM image from the dark contrast region showing the interfaces between BST and pure Te. m) HAADF STEM image acquired from the interface of two nanoflakes that have merged.

[110] zone axis.^[51] After annealing, the BT quintuple layers at the interface apparently disintegrate into a Te-deficient BiTe phase. Compared with the as-prepared BT thin films that are only partially

connected by surface steps, adjacent nanoflakes in the annealed sample are connected via BiTe phase, which can increase the electrical conductivity. This interfacial reaction creates new interfaces between the BT

quintuple layers and BiTe, providing extra interfacial scattering that can potentially influence the electrical conductivity.^[52]

We then investigated the influence of Sb doping on the microstructure of the (0001) surface. The as-prepared BST thin film with $x = 0.2$ has a microstructure very similar to the as-prepared BT thin film. The nanoflake thickness is 12 ± 6 nm, which is similar to that of the BT sample. The (0001) interfaces between the BST nanoflakes show a blurry contrast, which is related to a Sb signal in the EDS elemental mapping (Figure 4f). The presence of Sb is also detected at the endpoints between two nanoplates and other filling regions (Figure 4f, Figure S7, Supporting Information). Apparently, Sb dopants tend to accumulate at the nanoplate surfaces (Figure 4k), which is consistent with previous report that it is easier to form Bi_2Te_3 than Sb_2Te_3 under hydrothermal conditions.^[40] The nanoflakes initially form Bi_2Te_3 , but as Bi in the solution becomes depleted, Sb and Te will form a compound at the surface. Atomic-resolution HAADF STEM shows that the (0001) interface has an fcc (Bi, Sb)Te structure (Figure 4g), similar to the annealed undoped sample (Figure 3h). Additionally, the presence of pure Te is observed at the endpoints of the nanoplates (Figure 4h). The pure Te epitaxially grows on the plate, exhibiting the following orientation relationship: $(0001)_{\text{BST}} // (0001)_{\text{Te}}$ and $[2\bar{1}\bar{1}0]_{\text{BST}} // [2\bar{1}\bar{1}0]_{\text{Te}}$. Surprisingly, even before annealing, Sb-doped BST flakes have complex phases at the interfaces, indicating that Sb can modify the surface structure, influence the hydrothermal reaction and promote interfacial reactions between adjacent flakes.

All the Sb-doped samples were then annealed at the previously-optimized temperature of 623 K for 24 h. For $x = 0.2$, after annealing, the nanoflakes become much thicker and the interface contrast significantly decreases (Figure 4i). The average thickness has increased from 12 to 16 nm (Figure 4j). Some nanoflakes seem to be the result of a merging of adjacent nanoflakes as their thickness is at least three times larger than the average thickness (Figure 4i). A typical feature in those thick nanoflakes is the presence of dark-contrast regions at the two ends. They contain parallel planar defects with an even darker contrast. EDS confirms that these dark regions are Sb-rich (Figure 4k). Atomic-resolution STEM confirms that the dark regions are mainly Sb-rich BST and the dark planar defects are pure Te aligned along the $[2\bar{1}\bar{1}0]$ zone axis (Figure 4l). Again the orientation relationship $(0001)_{\text{BST}} // (0001)_{\text{Te}}$ and $[2\bar{1}\bar{1}0]_{\text{BST}} // [2\bar{1}\bar{1}0]_{\text{Te}}$ was observed at the BST/Te interface. The merging between two flakes was captured using HAADF STEM (Figure 4m). The interface region now consists of three BST quintuple layers that have a misalignment from left to right. It is likely that annealing can reduce the twist angle between the adjacent nanoflakes as they merge to a thicker one.

All the Sb-doped samples are n-type which agrees with previous report that Sb needs to reach $x = 1.1$ for the film to convert from n-type to p-type.^[32] As the Sb content increases, the electrical conductivity increases and reaches a maximum of 9.75 S m^{-1} for $x = 0.2$ at room temperature, which is 49.7% higher than the undoped sample (6.51 S m^{-1}). This can be attributed to the Sb-enhanced out-of-plane connectivity between (0001) interfaces, and the in-plane connectivity between horizontal nanoflakes. When the Sb content further increases to 0.4, the electrical conductivity starts to decrease. Excessive Sb may facilitate the formation of Sb'_{Te} antisite defects,^[53–55] which creates holes, and decreases the electron carrier concentration. Another reason could be the formation of pure Te, which suppresses formation of Te vacancies in the BST nanoflakes, decrease electron carrier concentration, and then decrease electrical conductivity. The extra scattering from Sb'_{Te} may also cause the electrical conductivity to decrease. The Seebeck

coefficient reaches its maximum value of $145 \mu\text{V K}^{-1}$ at $x = 0.1$ and $T = 400$ K. However, the maximum Seebeck coefficient of BST is rather independent on the Sb concentration and remains quite stable for different x values ($140\text{--}145 \mu\text{V K}^{-1}$). Apparently, the main gain in Seebeck coefficient is from the annealing process, while the influence of Sb doping is secondary. It has been reported that the Te/BST heterostructure can push the Fermi level closer to the conduction band, which might be the reason for the enhanced Seebeck coefficient.^[34] The power factor (Figure 4c) increases first and then decreases with the increase of Sb content and reaches a peak of $1.72 \text{ mW m}^{-1} \text{ K}^{-2}$ at $x = 0.2$ and $T = 343$ K. Compared with the value of $1.2 \text{ mW m}^{-1} \text{ K}^{-2}$ at $x = 0$, the power factor has increased by about 43.3%. It is speculated that the new interfaces between BST/BiTe and BST/Te created by annealing and doping can reduce lattice thermal conductivity. The Sb dopants in the lattice can also reduce lattice thermal conductivity. Overall, doping should reduce the lattice thermal conductivity of the thin film.

3. Conclusion

BST thin films with a controllable (0001) interface were synthesized using a spin coating method. The microstructure of the (0001) interface in BST samples with different Sb content and different annealing temperature was investigated using atomic-resolution STEM, which allowed us to understand the enhancement of the electrical transport properties of the BST thin films. A maximum power factor of $1.72 \text{ mW m}^{-1} \text{ K}^{-2}$ was obtained; 43.3% higher than that of a pure Bi_2Te_3 thin film. This approach provides new opportunities to unravel the complicated structure–property relationship at interfaces and helps to design TE materials with an optimized interface structure.

4. Materials and Methods

Hydrothermal synthesis of $\text{Bi}_{2-x}\text{Sb}_x\text{Te}_3$ nanoflakes: The 3 mmol Na_2TeO_3 , $2-x$ mmol BiCl_3 , x mmol SbCl_3 ($x = 0, 0.1, 0.2, 0.4$), 0.7 g NaOH, 1 g PVP, and 70 mL ethylene glycol (EG) were mixed using magnetic stirrer.^[56] BiCl_3 , SbCl_3 , and PVP were purchased from Alfa Aesar. Na_2TeO_3 , NaOH, and EG were purchased from Shanghai Chemical Reagents Co. Ltd. All chemicals are analytical grade. The solution was then transferred to a stainless-steel reactor lined with polytetrafluoroethylene with a capacity of 100 mL, sealed and heated to 180°C for 24 h, and finally cooled to room temperature. After adding 30 mL anhydrous ethanol, the mixture was centrifuged at $7155 g$ for 5 min. The supernatant is removed and the solid is dispersed in a centrifuge tube by ultrasonic treatment. The nanoflakes were washed using deionized water for two times and anhydrous ethanol for one time. The final product was dispersed in anhydrous ethanol.

Preparation of flexible $\text{Bi}_{2-x}\text{Sb}_x\text{Te}_3$ nanoflake film: The $\text{Bi}_{2-x}\text{Sb}_x\text{Te}_3$ nanoflakes in anhydrous ethanol were first dispersed using ultrasound. Then the solution was spin-coated onto a polyimide substrate that rotates at 2500–3500 rpm. The desired film thickness can be obtained by controlling the dispersion concentration and spin coating time. Finally, heat treatment was performed in a tube furnace under argon atmosphere at $300\text{--}350^\circ\text{C}$ ($573\text{--}623$ K) for 1 h.

Characterization: The crystal structure of $\text{Bi}_{2-x}\text{Sb}_x\text{Te}_3$ nanoflakes was characterized by X-ray diffractometer (XRD, Smart Lab) using $\text{Cu K}\alpha$ ($\lambda = 0.1514186$ nm). Microstructure characterization was performed using a field emission scanning electron microscopy (FESEM) (JEM-SU8020). The chemical composition was analyzed using X-ray photoelectron spectroscopy (XPS). Transmission electron microscope (TEM) samples were prepared using Helios NanoLab G3 UC focused ion beam (FIB). STEM characterization was performed using a Thermo Fisher double aberration-corrected Titan Themis operated at 300 kV and equipped with four SDD EDS detectors. High angle annular dark field (HAADF)

STEM images were acquired using a Fishione HAADF detector with an inner angle of 48 mrad and outer angle of 200 mrad.

The electrical conductivity (σ) and Seebeck coefficient (α) were measured using a four-probe method to reduce influence from contact resistance, on a CTA instrument (Cryoall Company, Beijing). The Seebeck coefficient was obtained by heating up the sample to produce a stable temperature gradient and then using the probes to detect the voltage difference ΔV and temperature difference ΔT simultaneously, according to the definition $\alpha = \Delta V / \Delta T$.

Acknowledgements

X.W. and J.D. contributed equally to this work. This work was supported by the National Natural Science Foundation of China (52272235). The S/TEM work was performed at the Nanostructure Research Center (NRC), which was supported by the Fundamental Research Funds for the Central Universities (WUT: 2021III016GX).

Conflict of Interest

The authors declare no conflict of interest.

Supporting Information

Supporting Information is available from the Wiley Online Library or from the author.

Keywords

Bi_2Te_3 nanoflakes, interface engineering, scanning transmission electron microscopy, thermoelectric thin film

Received: February 14, 2024

Revised: March 10, 2024

Published online: March 16, 2024

- [1] A. K. Geim, I. V. Grigorieva, *Nature* **2013**, 499, 419.
- [2] X. Duan, C. Wang, J. C. Shaw, R. Cheng, Y. Chen, H. Li, X. Wu, Y. Tang, Q. Zhang, A. Pan, J. Jiang, R. Yu, Y. Huang, X. Duan, *Nat. Nanotechnol.* **2014**, 9, 1024.
- [3] Z. Zhou, F. Hou, X. Huang, G. Wang, Z. Fu, W. Liu, G. Yuan, X. Xi, J. Xu, J. Lin, L. Gao, *Nature* **2023**, 621, 499.
- [4] Q. Jin, S. Jiang, Y. Zhao, D. Wang, J. Qiu, D. M. Tang, J. Tan, D. M. Sun, P. X. Hou, X. Q. Chen, K. Tai, N. Gao, C. Liu, H. M. Cheng, X. Jiang, *Nat. Mater.* **2019**, 18, 62.
- [5] K. S. Burch, D. Mandrus, J. G. Park, *Nature* **2018**, 563, 47.
- [6] M. Gibertini, M. Koperski, A. F. Morpurgo, K. S. Novoselov, *Nat. Nanotechnol.* **2019**, 14, 408.
- [7] C. Li, S. Ma, P. Wei, W. Zhu, X. Nie, X. Sang, Z. Sun, Q. Zhang, W. Zhao, *Energy Environ. Sci.* **2020**, 13, 535.
- [8] K. S. Novoselov, A. K. Geim, S. V. Morozov, D. Jiang, Y. Zhang, S. V. Dubonos, I. V. Grigorieva, A. A. Firsov, *Science* **2004**, 306, 666.
- [9] M. C. Lemme, D. Akinwande, C. Huyghebaert, C. Stampfer, *Nat. Commun.* **2022**, 13, 1392.
- [10] E. Y. Tsybal, *Science* **2021**, 372, 1389.
- [11] Y. Cao, V. Fatemi, S. Fang, K. Watanabe, T. Taniguchi, E. Kaxiras, P. Jarillo-Herrero, *Nature* **2018**, 556, 43.
- [12] M. Chen, X. Chen, H. Yang, Z. Du, H. Wen, *Sci. Adv.* **2018**, 4, 7.
- [13] R. Deng, X. Su, S. Hao, Z. Zheng, M. Zhang, H. Xie, W. Liu, Y. Yan, C. Wolverton, C. Uher, M. G. Kanatzidis, X. Tang, *Energy Environ. Sci.* **2018**, 11, 1520.
- [14] Q. Zhang, X. Ai, L. Wang, Y. Chang, W. Luo, W. Jiang, L. Chen, *Adv. Funct. Mater.* **2015**, 25, 966.
- [15] B. Qin, D. Wang, X. Liu, Y. Qin, J. F. Dong, J. Luo, J. W. Li, W. Liu, G. Tan, X. Tang, J. F. Li, J. He, L. D. Zhao, *Science* **2021**, 373, 556.
- [16] C. Zhang, Z. Peng, Z. Li, L. Yu, K. A. Khor, Q. Xiong, *Nano Energy* **2015**, 15, 688.
- [17] Y. Zheng, T. J. Slade, L. Hu, X. Y. Tan, Y. Luo, Z. Z. Luo, J. Xu, Q. Yan, M. G. Kanatzidis, *Chem. Soc. Rev.* **2021**, 50, 9022.
- [18] Y. Lu, Y. Zhou, W. Wang, M. Hu, X. Huang, D. Mao, S. Huang, L. Xie, P. Lin, B. Jiang, B. Zhu, J. Feng, J. Shi, Q. Lou, Y. Huang, J. Yang, J. Li, G. Li, J. He, *Nat. Nanotechnol.* **2023**, 18, 1281.
- [19] Y. Yu, X. Xu, Y. Wang, B. Jia, S. Huang, X. Qiang, B. Zhu, P. Lin, B. Jiang, S. Liu, X. Qi, K. Pan, D. Wu, H. Lu, M. Bosman, S. J. Pennycook, L. Xie, J. He, *Nat. Commun.* **2022**, 13, 5612.
- [20] D. Su, J. Cheng, S. Li, S. Zhang, T. Lyu, C. Zhang, J. Li, F. Liu, L. Hu, J. Mater. Sci. Technol. **2023**, 138, 50.
- [21] S. He, A. Bahrami, X. Zhang, I. G. Martínez, S. Lehmann, K. Nielsch, *Adv. Mater. Technol.* **2022**, 7, 2100953.
- [22] S. He, J. Yang, A. Bahrami, X. Zhang, R. He, M. Hantusch, S. Lehmann, K. Nielsch, *ACS Appl. Energy Mater.* **2022**, 5, 4041.
- [23] S. Lehmann, F. Mitzscherling, S. He, J. Yang, M. Hantusch, K. Nielsch, A. Bahrami, *Coatings* **2023**, 13, 641.
- [24] K. C. Kim, S. S. Lim, S. H. Lee, J. Hong, D. Y. Cho, A. Y. Mohamed, C. M. Koo, S. H. Baek, J. S. Kim, S. K. Kim, *ACS Nano* **2019**, 13, 7146.
- [25] C. Wan, R. Tian, M. Kondou, R. Yang, P. Zong, K. Koumoto, *Nat. Commun.* **2017**, 8, 1024.
- [26] R. Nunna, P. Qiu, M. Yin, H. Chen, R. Hanus, Q. Song, T. Zhang, M. Y. Chou, M. T. Agne, J. He, G. J. Snyder, X. Shi, L. Chen, *Energy Environ. Sci.* **2017**, 10, 1928.
- [27] G. Han, W. Zhu, S. Guo, J. Zhou, Y. Liu, Y. Deng, *J. Mater. Sci. Technol.* **2023**, 160, 18.
- [28] W. Liu, S. Bai, *J. Mater.* **2019**, 5, 321.
- [29] L. Xie, L. Yin, Y. Yu, G. Peng, S. Song, P. Ying, S. Cai, Y. Sun, W. Shi, H. Wu, N. Qu, F. Guo, W. Cai, H. Wu, Q. Zhang, K. Nielsch, Z. Ren, Z. Liu, J. Sui, *Science* **2023**, 382, 921.
- [30] B. Poudel, Q. Hao, Y. Ma, Y. Lan, A. Minnich, B. Yu, X. Yan, D. Wang, A. Muto, D. Vashaee, X. Chen, J. Liu, M. S. Dresselhaus, G. Chen, Z. Ren, *Science* **2008**, 320, 634.
- [31] C. Hollar, Z. Lin, M. Kongara, T. Varghese, C. Karthik, J. Schimpf, J. Eixenberger, P. H. Davis, Y. Wu, X. Duan, Y. Zhang, D. Estrada, *Adv. Mater. Technol.* **2020**, 5, 2000600.
- [32] B. Du, J. Wu, X. Lai, Y. Deng, S. Wang, H. Liu, J. Liu, J. Jian, *Ceram. Int.* **2019**, 45, 3244.
- [33] S. He, S. Lehmann, A. Bahrami, K. Nielsch, *Adv. Energy Mater.* **2021**, 11, 2101877.
- [34] M. Hong, Z. Chen, L. Yang, J. Zou, *Nanoscale* **2016**, 8, 8681.
- [35] M. Hong, Z. G. Chen, L. Yang, G. Han, J. Zou, *Adv. Electron. Mater.* **2015**, 1, 1500025.
- [36] M. Hong, Z. G. Chen, L. Yang, J. Zou, *Nano Energy* **2016**, 20, 144.
- [37] X. Mu, H. Zhou, D. He, W. Zhao, P. Wei, W. Zhu, X. Nie, H. Liu, Q. Zhang, *Nano Energy* **2017**, 33, 55.
- [38] L. Hu, H. Wu, T. Zhu, C. Fu, J. He, P. Ying, X. Zhao, *Adv. Energy Mater.* **2015**, 5, 1500411.
- [39] O. L. Krivanek, M. F. Chisholm, V. Nicolosi, T. J. Pennycook, G. J. Corbin, N. Dellby, M. F. Murfitt, C. S. Own, Z. S. Szilagy, M. P. Oxley, S. T. Pantelides, S. J. Pennycook, *Nature* **2010**, 464, 571.
- [40] J. Mi, P. Norby, M. Bremholm, B. B. Iversen, *Chem. Mat.* **2017**, 29, 5070.
- [41] W. Cui, W. Lin, W. Lu, C. Liu, Z. Gao, H. Ma, W. Zhao, G. van Tendeloo, W. Zhao, Q. Zhang, X. Sang, *Nat. Commun.* **2023**, 14, 554.
- [42] X. Sang, Y. Xie, D. E. Yilmaz, R. Lotfi, M. Alhabeab, A. Ostadhosseini, B. Anasori, W. Sun, X. Li, K. Xiao, P. R. C. Kent, A. C. T. van Duin, Y. Gogotsi, R. R. Unocic, *Nat. Commun.* **2018**, 9, 2266.
- [43] X. Sang, X. Li, W. Zhao, J. Dong, C. M. Rouleau, D. B. Geohegan, F. Ding, K. Xiao, R. R. Unocic, *Nat. Commun.* **2018**, 9, 2051.

- [44] X. Sang, E. D. Grimley, C. Niu, D. L. Irving, J. M. LeBeau, *Appl. Phys. Lett.* **2015**, *106*, 061101.
- [45] H. Wang, F. Liu, R. Yu, J. Wu, *Interdiscip. Mater.* **2022**, *1*, 196.
- [46] A. A. Volykhov, J. Sánchez-Barriga, A. P. Sirotnina, V. S. Neudachina, A. S. Frolov, E. A. Gerber, E. Y. Kataev, B. Senkovsky, N. O. Khmelevsky, A. Y. Aksenenko, N. V. Korobova, A. Knop-Gericke, O. Rader, L. V. Yashina, *Chem. Mat.* **2016**, *28*, 8916.
- [47] R. J. Macedo, S. E. Harrison, T. S. Dorofeeva, J. S. Harris, R. A. Kiehl, *Nano Lett.* **2015**, *15*, 4241.
- [48] W. Lu, W. Cui, W. Zhao, W. Lin, C. Liu, G. van Tendeloo, X. Sang, W. Zhao, Q. Zhang, *Adv. Mater. Interfaces* **2022**, *9*, 2102161.
- [49] Y. Chen, X. Nie, C. Sun, S. Ke, W. Xu, Y. Zhao, W. Zhu, W. Zhao, Q. Zhang, *Adv. Funct. Mater.* **2022**, *32*, 2111373.
- [50] F. Liu, M. Zhang, P. Nan, X. Zheng, Y. Li, K. Wu, Z. Han, B. Ge, X. Zhao, C. Fu, T. Zhu, *Small Sci.* **2023**, DOI: [10.1002/smssc.202300082](https://doi.org/10.1002/smssc.202300082).
- [51] K. Park, K. Ahn, J. Cha, S. Lee, S. I. Chae, S. P. Cho, S. Ryee, J. Im, J. Lee, S. D. Park, M. J. Han, I. Chung, T. Hyeon, *J. Am. Chem. Soc.* **2016**, *138*, 14458.
- [52] C. Hu, K. Xia, C. Fu, X. Zhao, T. Zhu, *Energy Environ. Sci.* **2022**, *15*, 1406.
- [53] J. Zhang, W. Ming, Z. Huang, G.-B. Liu, X. Kou, Y. Fan, K. L. Wang, Y. Yao, *Phys. Rev. B* **2013**, *88*, 235131.
- [54] M. Tan, X. L. Shi, W. D. Liu, M. Li, Y. Wang, H. Li, Y. Deng, Z. G. Chen, *Adv. Energy Mater.* **2021**, *11*, 2102578.
- [55] Y. Xu, Y. Zhou, X. D. Wang, W. Zhang, E. Ma, V. L. Deringer, R. Mazzarello, *Adv. Mater.* **2022**, *34*, 2109139.
- [56] Y. Zhang, L. Hu, T. Zhu, J. Xie, X. Zhao, *Cryst. Growth Des.* **2013**, *13*, 645.